Investigating line- versus point-laser excitation for three-dimensional fluorescence imaging and tomography employing a trimodal imaging system

Liji Cao
Jörg Peter

Investigating line- versus point-laser excitation for three-dimensional fluorescence imaging and tomography employing a trimodal imaging system

Liji Cao and Jörg Peter
German Cancer Research Center, Department of Medical Physics in Radiology, Heidelberg, Germany

Abstract. The adoption of axially oriented line illumination patterns for fluorescence excitation in small animals for fluorescence surface imaging (FSI) and fluorescence optical tomography (FOT) is being investigated. A trimodal single-photon-emission-computed-tomography/computed-tomography/optical-tomography (SPECT-CT-OT) small animal imaging system is being modified for employment of point- and line-laser excitation sources. These sources can be arbitrarily positioned around the imaged object. The line source is set to illuminate the object along its entire axial direction. Comparative evaluation of point and line illumination patterns for FSI and FOT is provided involving phantom as well as mouse data. Given the trimodal setup, CT data are used to guide the optical approaches by providing boundary information. Furthermore, FOT results are also being compared to SPECT. Results show that line-laser illumination yields a larger axial field of view (FOV) in FSI mode, hence faster data acquisition, and practically acceptable FOT reconstruction throughout the whole animal. Also, superimposed SPECT and FOT data provide additional information on similarities as well as differences in the distribution and uptake of both probe types. Fused CT data enhance further the anatomical localization of the tracer distribution *in vivo*. The feasibility of line-laser excitation for three-dimensional fluorescence imaging and tomography is demonstrated for initiating further research, however, not with the intention to replace one by the other. © *The Authors. Published by SPIE under a Creative Commons Attribution 3.0 Unported License. Distribution or reproduction of this work in whole or in part requires full attribution of the original publication, including its DOI.* [DOI: 10.1117/1.JBO.18.6.066015]

Keywords: fluorescence imaging; fluorescence optical tomography; line laser; single photon emission computed tomography; x-ray computed tomography; multimodal imaging.

Paper 130163R received Mar. 21, 2013; revised manuscript received May 17, 2013; accepted for publication May 17, 2013; published online Jun. 24, 2013.

1 Introduction

Spatially resolved detection of fluorescence-labeled agent distribution in mice has been demonstrated to hold great potential in a broad spectrum of preclinical molecular imaging studies.[1] Because of the mathematical difficulties in resolving the highly scattering nature of light photon propagation in tissue, the majority of *in vivo* small animal fluorescence imaging applications in the laboratory settings is mostly performed to generate two-dimensional (2-D) planar images following epi-illumination.[2] Nonetheless, to improve localization as well as to enable quantification of fluorescent sources, efforts have been taken toward fully three-dimensional (3-D) tomographic reconstruction of fluorescence light distribution within heterogeneously turbid and arbitrarily shaped objects such as mice and, in some cases, up to the size of rats.[3,4]

Noncontact data acquisition approaches have replaced fiber-based contact imaging implementations for the most part mainly because of animal handling and efficiency shortcomings of the latter.[5] Some noncontact imaging systems perform fluorescence optical tomography (FOT) reconstruction by slightly squeezing the imaged animal into, or between, a purposely shaped chamber of simple geometry (e.g., translucent vices),[6,7] or within translucent compartments of (generally) cylindrical geometry

with lesser spacing constraints forced onto the animal.[8,9] Planar spacing by the use of opposite vices yields a much reduced boundary complexity involved in solving the inverse problem. However, this method substantially restricts freedom of excitation and detection geometry. Cylindrical animal burrow enclosures maintain a "normal" body shape and allow for arbitrary excitation and detection from the full set of 360 deg source angles and imaging projections.[8,9] However, this geometry involves a rather complex problem space for the inverse problem. The imaging system embodied herein uses the latter approach incorporating an animal enclosure with a bore holder of 30-mm inner diameter. Fluorescence surface imaging (FSI) is performed by illuminating the entire imaged object, or local regions thereof, with a large, preferably homogeneous field of light to excite fluorochromes in a large area, generally the whole animal.

In almost all noncontact FOT approaches, though, laser beam generated point illumination is used to sequentially form an illumination pattern on the surface of the animal to create a sufficiently high number of source points on the surface, which are paired with some data projection schema, respectively.[10] Such scanning strategy, however, can be time consuming. Adoption of galvanometer mirrors as suggested by Patwardhan et al. can accelerate the scanning process.[11] This strategy, however, still induces a large amount of acquired data and, hence, yields a large space problem for the FOT image reconstruction. Following recent studies, wide field illumination using structured light or spatially modulated light has been extensively investigated for turbid media as well as for *in vivo* imaging.[12–16]

Address all Correspondence to: Liji Cao, German Cancer Research Center (DKFZ), Department of Medical Physics in Radiology, E020, Im Neuenheimer Feld 280, D-69120 Heidelberg, Germany. Tel: +49 6221 42 2606; Fax: +49 6221 42 2585; E-mail: l.cao@dkfz.de.

Those interesting approaches are intended for lessening the inherently ill-posed nature of FOT[12–14] or lowering the number of excitation points.[15,16]

In the present study, we seek to investigate the use of single excitation line illumination as generated by a line laser source and conduct comparative experiments for FSI and FOT. The line source is fit and aligned with the axial center line of the imaging bore and rotationally mounted at some distance from the imaged object. Hence, a single 360-deg revolution (at certain angular stepping offsets) of the line source forms an illumination pattern along with a set of projection data that could be used for both FSI and FOT.

Combining *in vivo* optical imaging with further imaging modalities such as CT is being adopted more and more to improve reconstruction accuracy and, hence, signal localization.[17–19] To conduct this study, the optical imaging setup, including all light sources, is for that reason placed into a trimodal small animal imaging system, incorporating also CT and SPECT.[20] This enables simultaneous, coregistered FSI and FOT imaging with CT and SPECT.

2 Materials and Methods

2.1 Imaging System

In the given trimodal embodiment, cf. Fig. 1(a) and 1(b), the optical imaging part is composed of a light camera (ORCA-AG, Hamamatsu Photonics, Shizuoka, Japan) and two fitted laser diode sources for probe excitation: (1) a collimated point-laser with 20 mW power at 660 nm (FP-66/20AAF-AV, Laser Components GmbH, Olching, Germany) and (2) a collimated line-laser with 70 mW power at 660 nm (FP-66/70LF-Ö90-HOM, Laser Components GmbH, Olching, Germany). The point laser diode is aligned and can be shifted parallel to the long axis of the imaged object. Hence, any point radial along

the long axis can be illuminated [Fig. 1(c) left]. The line laser beam is aligned with the axial long axis of the bore, as well. Its light field has a minimum length of 100 mm within a radius of 25 mm, hence illuminating a whole mouse [Fig. 1(c) right]. For all data acquisition studies conducted herein, a filter set combining a long-pass filter (RG695, Schott AG, Mainz, Germany) and a bandpass filter (FF01-716/40-25, Semrock Inc., Rochester, NY) is attached to the camera, and two bandpass filters (FF01-655/40-25, Semrock Inc., Rochester, NY) are fixed to the two laser sources, therefore enabling the acquisition of probes such as Cy5.5, DyLight 680, or Alexa Fluor 680.

The x-ray CT imaging part is composed of an x-ray tube having a 47.8 μm beam focus (Apogee Series 500, Oxford Instruments, Oxfordshire, UK) that is aligned to a flat panel x-ray detector (Shad-o-Box 2048, Rad-icon, Sunnyvale, CA) featuring a 2048×1024 pixel array with 48 μm pixel size. Three-dimensional images are reconstructed employing the Feldkamp–Davis–Kress (FDK) algorithm.[21]

To accomplish SPECT imaging a self-build gamma camera is used incorporating pixelated NaI(Tl) crystals of $1.3 \times 1.3 \times 6.0$ mm³ in size, arranged on a 66×66 array with 1.5 mm pixel spacing, the crystal array being fitted to a 2×2 multianode PMT array (Hamamatsu H8500, Hamamatsu Photonics, Shizuoka, Japan). A slit-slat collimator as described in Ref. 22 is attached to the gamma camera enabling whole-body mouse imaging [axial field-of-view (FOV) = 100 mm]. Three-dimensional images are reconstructed employing the maximum-likelihood expectation-maximization algorithm.[23]

All imaging components are mounted on a common rotatable and translatable gantry, and share fully overlapping fields of view [Fig. 1(b)]. All subsystems are fully calibrated yielding intrinsically fused intermodal and FSI-FOT data.[24] Careful calibration is particularly essential not only for fused imaging representation and derived diagnostic interpretation, but
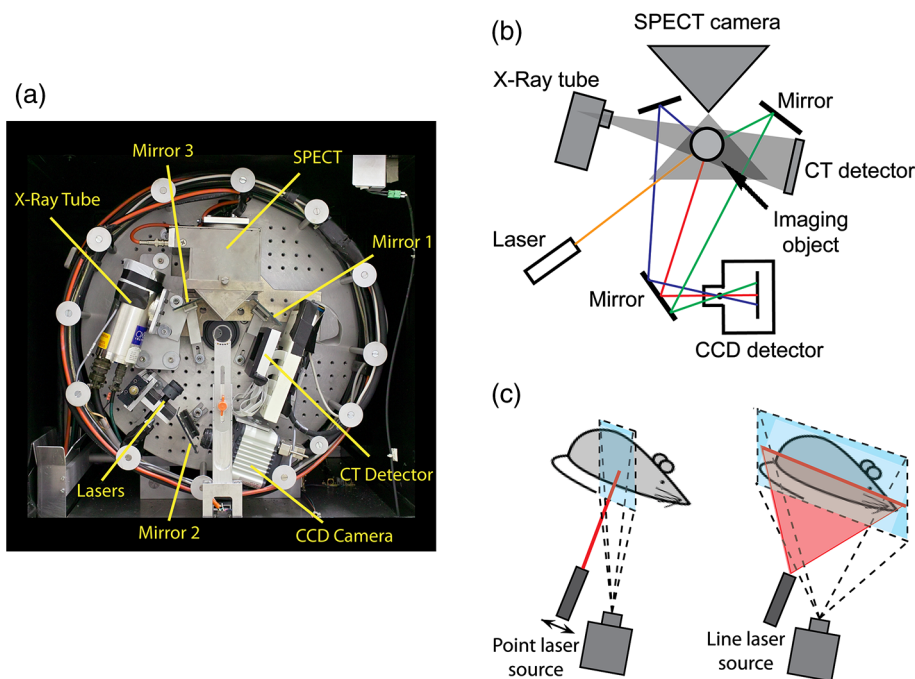

Fig. 1 (a) Front view of the trimodality SPECT–CT–OT small animal imaging system. (b) Illustration of the assembly and the overlapping FOVs of the three modalities. (c) Simplified illustration of the imaging FOV employing a point-laser (left) and an axially positioned line-laser (right) as the excitation light sources.

constitutes a crucial precondition for both FSI mapping and FOT reconstruction algorithms as laid out in the following.

2.2 3-D Fluorescence Surface Imaging

Figure 2 shows the flow diagram of the algorithm developed and used to obtain FSI data at each surface point of the 3-D object. In short, reconstructed x-ray CT data of the imaged object are segmented first by regional growing to provide the object's boundary shape. Detected fluorescence signals are then mapped onto the surface for every imaging angle over a 360-deg rotation according to the specific intermodal system geometry. Finally, cumulated FSI data are normalized with respect to the (possibly
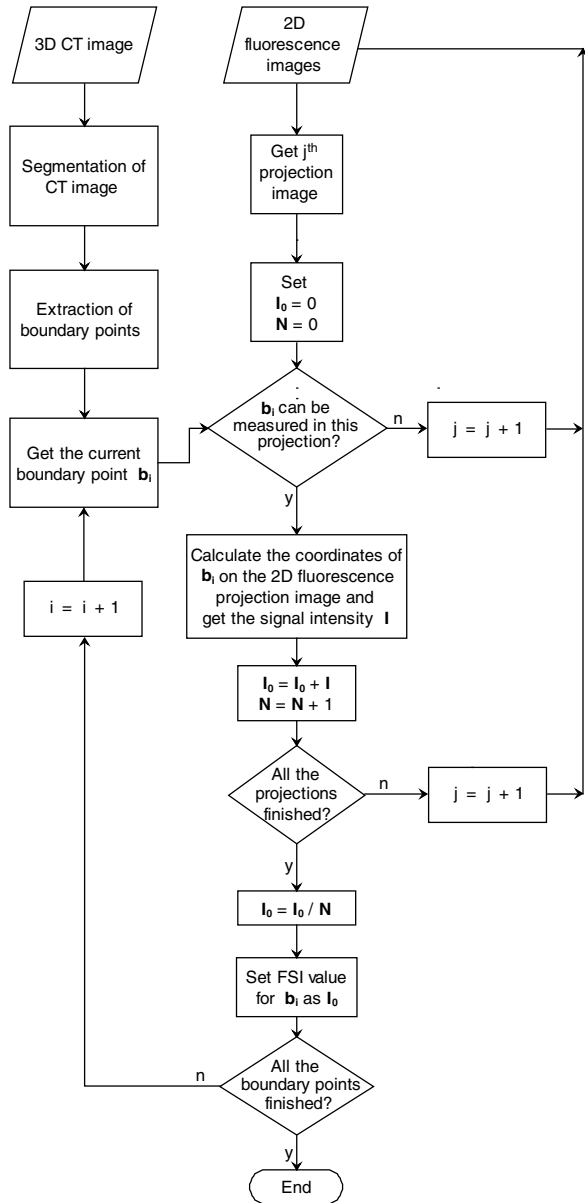

Fig. 2 Flow diagram of the mapping algorithm to generate a 3-D surface image with point- or line-laser excitation over 360 deg. In this algorithm, 3-D CT data are used to get all the boundary points $\mathbf{b}_i$. For each j'th 2-D fluorescence projection data, the mapped signal intensity $\mathbf{I_0}$ for each boundary point is added by the signal intensity $\mathbf{I}$ on the according position of the fluorescence image. Finally, the summed intensity $\mathbf{I_0}$ is normalized by the number of projection data $\mathbf{N}$.

varying) number of contributing light rays as illustrated in Fig. 2. This strategy is basically the same for either illumination pattern (point or line).

In order to visualize FSI data in the form of projectional views—which are similar and comparable to views from 2-D epi-illumination acquisitions—2-D projection images are digitally generated using the fused 3-D CT (printed in grayscale) and FSI (printed in pseudocolor) images at any arbitrarily chosen view angle (figures in Secs. 3.1.1 and 3.2.1 for the visualization results).

2.3 Fluorescence Optical Tomography

If point-laser source driven FOT is performed, then the 3-D image reconstruction algorithm as proposed and presented in Ref. 19 is being used. Three-dimensional tetrahedral meshes of the imaged object are generated from the boundary segmented CT data using the TetGen library.[25]

If, however, the line source illumination pattern is used for probe excitation, then a modified 2-D image reconstruction algorithm is used as described below to solve the inverse problem at any transversal plane of interest. Assuming that the line source excitation is homogeneous along its entire length, a stack of 2-D image reconstructions yields a volumetric (3-D) map of estimated fluorochrome distribution. Two-dimensional triangular meshes, generated at any transversal slice of interest, serve as the object's geometric representation. The 2-D image reconstruction algorithm has been derived from the 3-D algorithm as given in Ref. 19 whereby the propagation of photons inside the imaged object follows the solution of coupled 2-D diffusion equations at any transversal slice as illuminated by the line source which is expressed as

$$-\nabla \cdot [D\nabla\Phi_{ex}(\mathbf{r})] + \mu_a\Phi_{ex}(\mathbf{r}) = \Theta_s\delta(\mathbf{r} - \mathbf{r}_s)$$
$$-\nabla \cdot [D\nabla\Phi_{fl}(\mathbf{r})] + \mu_a\Phi_{fl}(\mathbf{r}) = \gamma\varepsilon c(\mathbf{r})\Phi_{ex}(\mathbf{r}), \qquad (1)$$

where $\mathbf{r} \in \mathbf{R}^2$ defines the position on the 2-D transaxial slice, $\Phi_{ex}(\mathbf{r})$ and $\Phi_{fl}(\mathbf{r})$ are the photon density distribution of excitation light and fluorescent light, respectively, $\mathbf{r}_s$ is the position of the intersection of the line laser and the current transaxial slice, Θ_s is the laser intensity; D and μ_a are the optical diffusion and absorption coefficients, which are assumed as homogeneous; and γ, ε, and $c(\mathbf{r})$ represent the quantum yield, the Molar extinction coefficient, and the concentration distribution of the fluorochrome probes, respectively. Such 2-D expression of diffusion equations is an approximation of the corresponding 3-D equations with the local assumption of

$$\frac{\partial\Phi_{ex}}{\partial z} = 0, \qquad \frac{\partial\Phi_{fl}}{\partial z} = 0, \qquad (2)$$

in which z defines the axial direction.

Assuming that $Y \in \mathbf{R}^{M \times 1}$ is the optical measurements for M detection positions and $X \in \mathbf{R}^{N \times 1}$ refers to the estimated fluorescence distribution at N mesh elements, the forward system model can be formulated as $Y = AX$, in which $A \in \mathbf{R}^{M \times N}$ is the system matrix calculated based on the numerical solution to Eq. (1) by the finite element method (FEM). The geometry used in FEM is based on 2-D meshes extracted from the corresponding CT data. Employing Tikhonov regularization, the corresponding reconstruction problem is formulated as

$$\min_{X \geq 0}\{\|Y - AX\|^2 + \lambda\|X\|^2\}, \tag{3}$$

in which λ is the parameter to control the regularization strength. The minimization problem is solved iteratively using the constrained conjugate gradient method which is constrained by enforcing nonnegativity.

2.4 Phantom Experiment

To validate the proposed method, a mouse-shaped phantom was adopted (XFM-2 Fluorescent Phantom, Caliper Life Science Inc., Hopkinton, MA; $\mu_a = 0.0047$ mm^{-1} and $D = 0.25$ mm). Two point sources filled with water solution of Cy5.5 Mono NHS Ester (approximately 40 pmol each; GE Healthcare, Buckinghamshire, UK) at the tips of two cylindrical rods

were inserted into the two holes of the phantom [Fig. 3(a)]. Figure 3(b) shows the exact positions of the two point sources in the phantom. CT data acquisition scans are first performed at 40 kV anode voltage, 0.4 mA tube current, 1 s acquisition time per projection, 240 projections per 360-deg rotation, whereby two axially shifted rotations are performed to cover an axial FOV of 100 mm. Following CT data acquisition, fluorescence data (60 projections per 360-deg rotation, 0.5 s exposure time per projection) were collected firstly employing point-laser excitation at seven axial positions (with axial intervals of 5 mm) with seven rotations, and thereafter employing line-laser excitation with a single rotation. For comparison, this phantom was also acquired by a self-built epi-illumination 2-D fluorescence imaging system which incorporates a CCD camera (ORCAII-BT-512G, Hamamatsu Photonics K.K., Hamamatsu City,
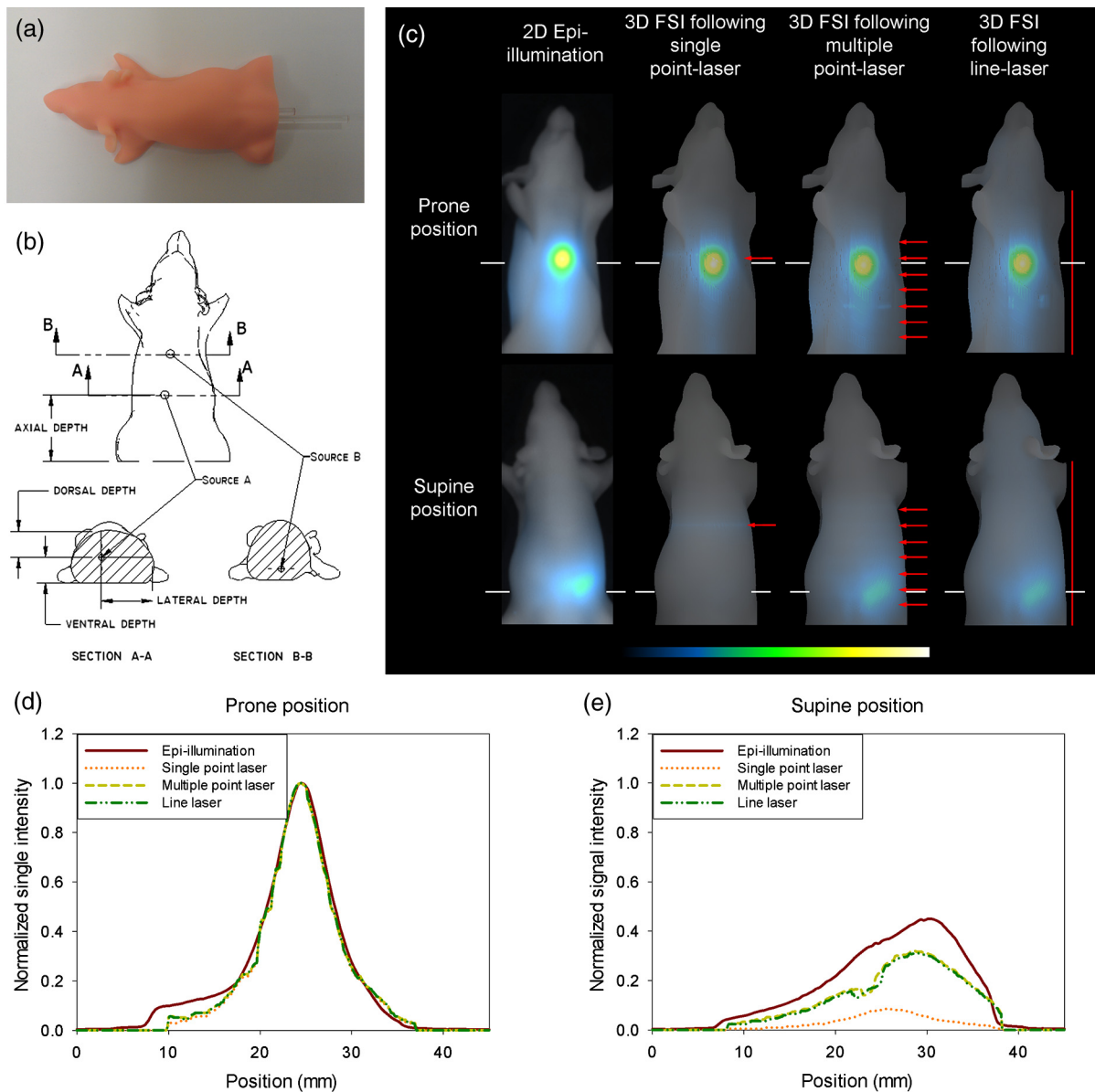

Fig. 3 (a) Photograph of the mouse-shaped phantom and (b) locations of the two fluorescent point sources in the phantom (courtesy of PerkinElmer Inc., Waltham, MA). (c) Results of 2-D epi-illumination acquisitions of the mouse phantom with prone and supine positions as well as the digitally generated projection views of 3-D FSI results acquired with point-laser (a single rotational scan and addition of seven rotational scans) and line-laser (a single rotation) excitations. Profiles of the normalized fluorescence signal intensity are given for the prone position (d) and the supine position (e) at the indicated locations [white lines in (c)].
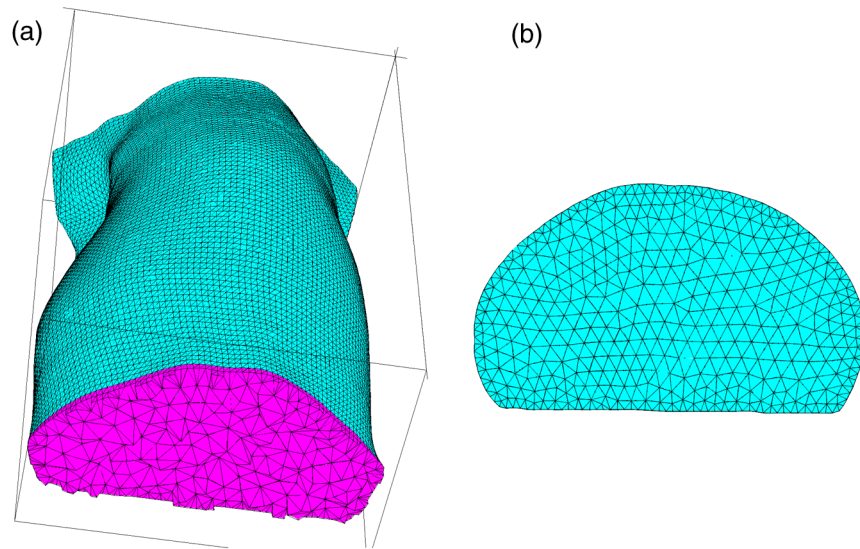
Fig. 4 (a) Partial view of the 3-D tetrahedral mesh derived from the phantom used in the 3-D image reconstruction algorithm for point-laser excitation. (b) Representative slice of a 2-D triangular mesh of the same phantom used in the 2-D image reconstruction algorithm for line source excitation.
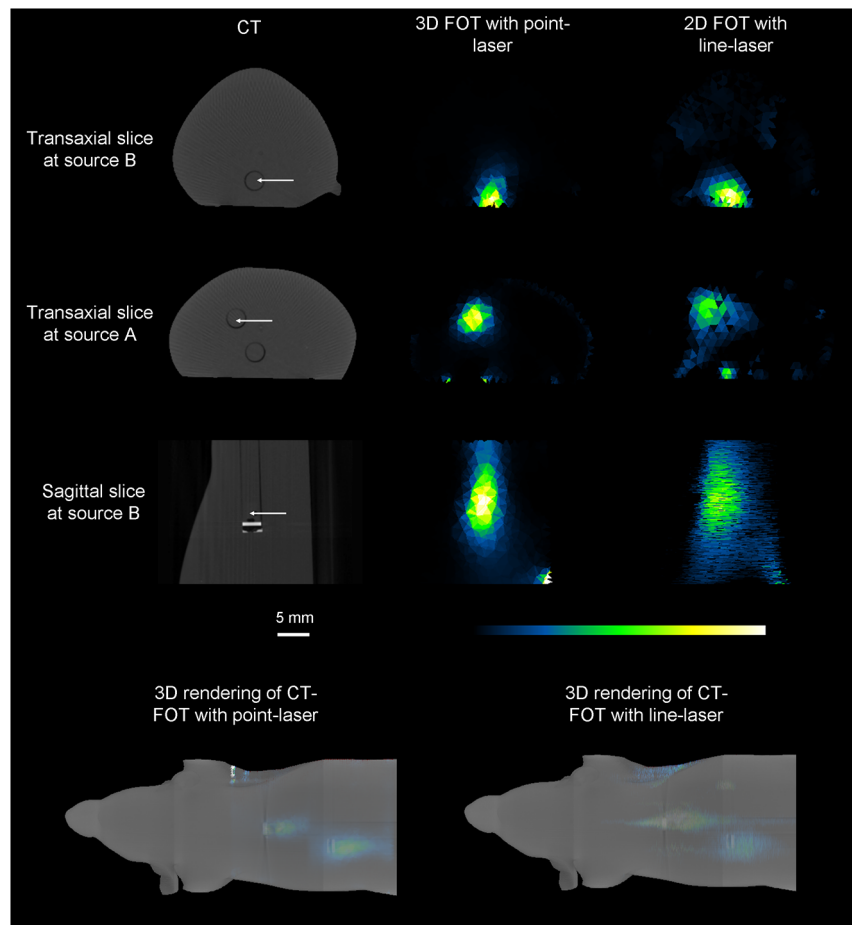

Fig. 5 Left: phantom CT images in transversal slices and a sagittal slice with indicated positions of two point fluorescent sources (arrows). Middle: 3-D FOT image reconstruction results following point-laser excitation. Right: 2-D FOT results following line-laser excitation. Three-dimensional rendering of CT-FOT with point-laser and line-laser illumination are shown at the bottom, respectively.

Japan) that is attached with an emission bandpass filter (FF01-716/40-25, Semrock Inc., Rochester, NY) as well as 4 LEDs (LR W5SM, OSRAM Opto Semiconductors GmbH, Regensburg, Germany) equipped with appropriate excitation filters (FF01-655/40-25, Semrock Inc., Rochester, NY).

2.5 In Vivo Mouse Experiment

To further demonstrate the preclinical imaging ability of the method, an *in vivo* mouse study was performed. This study was carried out according to the policies and principles established by the German animal protection laws of district government Karlsruhe with the animal number G-61/10. A healthy nude mouse was fed with chlorophyll free diets (CRD FLI, Harlan Laboratories, Inc., Indiana, IN) for three consecutive days prior to imaging to reduce autofluorescence from abdomen and skin. One day prior to imaging, the mouse was injected intravenously with 150 μl RediJect Bone Probe 680 (Caliper Life Science, Inc., Hopkinton, MA, concentration: 2 nmol/ 150 μl). For cross-validation, SPECT data (120 projections in a 360-deg rotation, 30 s per projection) have been collected

following the administration of 104 MBq ^{99m}Tc tagged to methylene diphosphonate molecules (MDP), injected 50 min prior to imaging. CT imaging was performed with the same protocol as described in the phantom experiment. Following SPECT and CT scans, fluorescence data were acquired (60 projections per 360-deg rotation, 0.5 s exposure time per projection), first employing point-laser excitation and, thereafter, employing line-laser excitation. Image reconstruction was performed in reference to every modality as previously described.

3 Results

3.1 Phantom Experiment Results

3.1.1 3-D FSI

Figure 3(c) shows results of 2-D epi-illumination acquisition of the mouse phantom at supine and prone positions, as well as digital 2-D projection views of fused 3-D CT and FSI data using both line-laser and point-laser illumination patterns, respectively. The view angles of the fused CT-FSI data are selected to be identical to those for the 2-D acquisition with
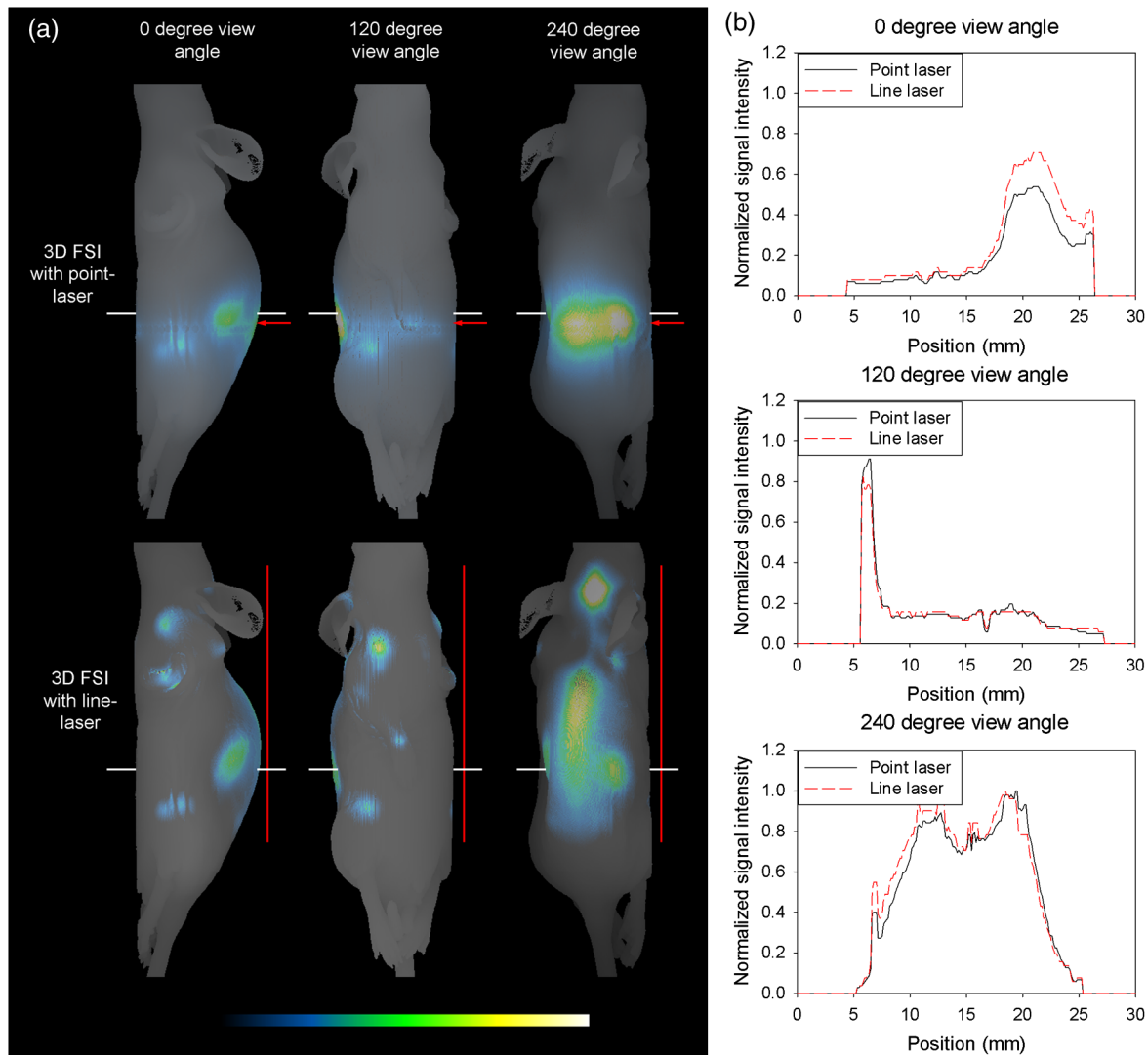

Fig. 6 (a) Digitally generated projection images of fused CT-FSI data at view angles of 0, 120, and 240 deg, respectively, following point-laser illumination (upper row) and line-laser illumination (lower row). (b) Normalized profiles of the fluorescence signal intensity at the indicated locations [white lines in (a)].

epi-illumination. As can be seen in Fig. 3(c), when 3-D FSI data are generated using point-laser illumination with only one axial position, the axial FOV is primarily covering one fluorescent point source. Using multiple point-laser or line-laser illumination, however, the whole phantom is exposed with one full rotation. The fluorescence signal intensities are normalized individually for each illumination strategy toward its maximum signal intensity. Figure 3(d) and 3(e) shows profiles of the signal intensities at the indicated positions providing quantitative comparison among different illumination types.

3.1.2 FOT

Figure 4(a) depicts part of the 3-D mesh as calculated from the acquired CT data. This data set includes 18,987 nodes and 73,339 tetrahedral elements. Figure 4(b) shows one of the derived 2-D meshes which includes 1017 nodes and 2593 triangular elements. Figure 5 shows results of 3-D FOT image reconstruction following point-laser excitation, alongside results of FOT 2-D image reconstruction following line-laser illumination; CT images are also provided as reference.

3.2 In Vivo Mouse Experiment Results

3.2.1 3-D FSI

The visualization of FSI results of the *in vivo* mouse experiment using digital projection data is shown in Fig. 6(a). The upper row demonstrates the results following point-laser illumination at a single axial position, while the lower row holds the results following line-laser illumination. Profiles of the normalized fluorescence signal intensities are shown in Fig. 6(b) for a more quantitative comparison between the results following both illumination patterns.

3.2.2 FOT

With regard to FOT image reconstruction, the optical properties of mouse tissue were assumed to be homogeneous with $\mu_a = 0.02$ mm^{-1} and $D = .24$ mm. In order to fuse the FOT data with the SPECT and CT results for diagnostic evaluation, the derived mesh geometries were reallocated into voxel-based representations at corresponding voxel resolutions. Results of 2-D FOT combining all slices are shown in Fig. 7 in the form of a maximum intensity projection view which is fused with SPECT–CT (left). CT, SPECT, 2-D FOT, and 3-D FOT data are also shown as transversal slices at the indicated axial positions (right).

4 Discussion

Mapping the fluorescence signals onto the surface and normalization over a 360-deg rotation (FSI mode) provides the opportunity to view the imaging results similar to a planar acquisition with epi-illumination, however, at any arbitrary view angle [see Figs. 3(c) and 6]. It has been shown that changing the view angle in 2-D optical data acquisition can affect the measured signal intensity. Three-dimensional FSI using line-laser illumination is, therefore, advantageous to 2-D epi-illumination acquisition by providing digital projection data at any required angular view.

Whole-body fluorescence imaging, especially FOT, is challenging because the probe often does not form unique spots but distributes widely throughout the body, particularly when systemic assessment is required, e.g., in a skeleton scan. Employing line-laser excitation enables one to perform whole-body fluorescence imaging at a much shorter scan time as compared to data acquisition strategies employing a point-laser source. Moreover, because of the extended excitation pattern throughout the axial direction generated by the line laser, the approximation of
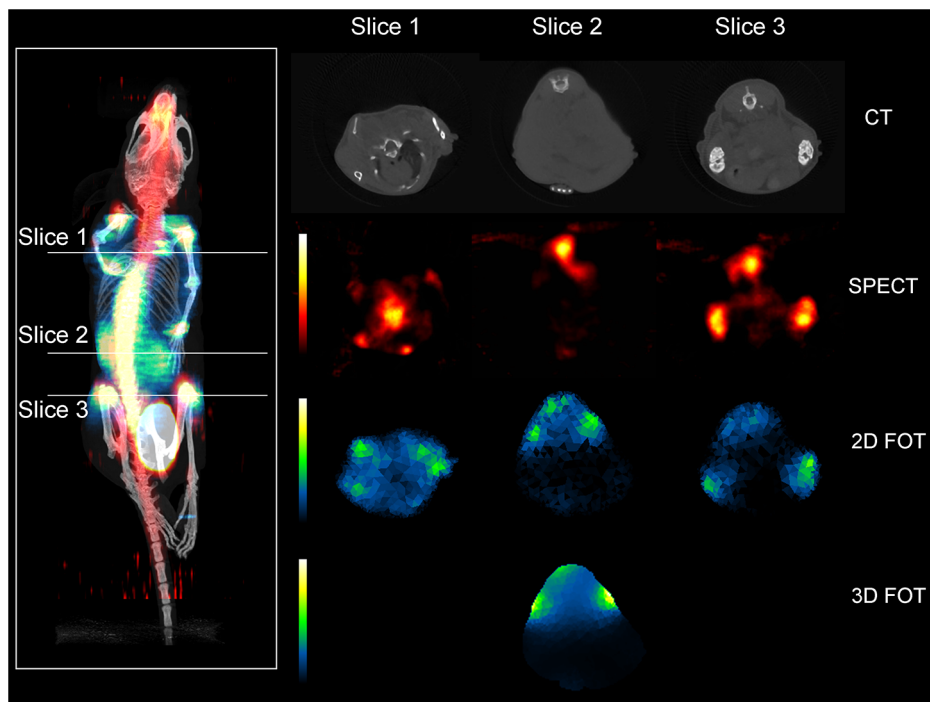

Fig. 7 Left: fused MIP view of reconstructed CT, SPECT, and 2-D FOT data. Right: reconstruction results for CT, SPECT, and 2-D FOT employing line-laser excitation at three indicated transaxial slices. The result of 3-D FOT employing point-laser excitation is shown at one slice position because of its limited axial FOV given a single rotational scan.

Eq. (2) could be locally held in practice. It is, however, not the case for point-laser illumination. Two-dimensional image reconstruction of tomographic slices becomes, therefore, practically available over the entire animal following line-laser excitation. In comparison to 3-D FOT reconstruction with point-laser excitation, this method allows a much larger FOV given the same acquisition time. In the mouse phantom study with two point-like fluorescence inclusions, the 2-D FOT result from the line-laser excitation shows broader distributions of the resolved point sources, especially in the axial direction, as compared to the 3-D reconstruction result from the point-laser excitation (cf. Fig. 5). Although, in this phantom study, 3-D FOT with point-laser outperforms 2-D FOT with line-laser excitation. Note, however, that the data acquisition time of the latter case was seven times faster. The *in vivo* experiment performed in this study is in fact an extremely challenging example for FOT as the hydroxyapatite-targeting probe has an affinity to the entire skeleton system in the animal which is very different to the case of spatially distinct point sources as are being used in the mouse phantom. The 2-D FOT reconstruction is applied slice by slice along the whole axial FOV. Intrinsically coregistered SPECT results with ^{99m}Tc-MDP, a probe with high bone-specificity as well, provides additional information for cross-validation. Two-dimensional FOT results are shown exemplarily in three different transaxial slices (cf. Fig. 7). It can be seen from "Slice 1" that the small bone structures close to surface are well resolved, while the spine, which shows a high activity uptake in SPECT, is not visible in FOT. In "Slice 2," the 2-D FOT image shows not only the spine structure near to the surface but also probe uptake in the kidneys, while no tracer activity can be seen in SPECT. "Slice 3" includes spine and knee joints, showing similar information in FOT and SPECT. Employing point-laser excitation, however, only a small portion of the animal is within the active FOV. The reconstruction results show a more pronounced convergence at the surface area (see the last row of Fig. 7).

This study has been particularly conducted to lay out a frame for future investigations. While exemplary studies have been provided illustratively for each illumination pattern, the results are not conclusive with respect to the quantitative accuracy of either of the involved method.

5 Conclusion

In conclusion, a trimodal SPECT–CT–OT system was investigated in this study, specifically with the aim of investigating the use of a line-laser as the excitation source for 3-D fluorescence imaging and tomography. Phantom and *in vivo* experiments demonstrate the feasibility of line-laser excitation yielding an axially enlarged FOV in both 3-D FSI and FOT with short acquisition time.

References

1. S. A. Hilderbrand and R. Weissleder, "Near-infrared fluorescence: application to in vivo molecular imaging," *Curr. Opin. Chem. Biol.* **14**(1), 71–79 (2010).

2. F. Leblond et al., "Pre-clinical whole-body fluorescence imaging: review of instruments, methods and applications," *J. Photochem. Photobiol. B* **98**(1), 77–94 (2010).

3. R. B. Schulz, J. Ripoll, and V. Ntziachristos, "Noncontact optical tomography of turbid media," *Opt. Lett.* **28**(18), 1701–1703 (2003).

4. A. Cong and G. Wang, "A finite-element-based reconstruction method for 3D fluorescence tomography," *Opt. Express* **13**(24), 9847–9857 (2005).

5. H. Meyer et al., "Noncontact optical imaging in mice with full angular coverage and automatic surface extraction," *Appl. Opt.* **46**(17), 3617–3627 (2007).

6. P. Mohajerani et al., "Compensation of optical heterogeneity-induced artifacts in fluorescence molecular tomography: theory and in vivo validation," *J. Biomed. Opt.* **14**(3), 034021 (2009).

7. K. O. Vasquez, C. Casavant, and J. D. Peterson, "Quantitative whole body biodistribution of fluorescent-labeled agents by non-invasive tomographic imaging," *PLoS One* **6**(6), e20594 (2011).

8. N. Deliolanis et al, "Free-space fluorescence molecular tomography utilizing 360 degrees geometry projections," *Opt. Lett.* **32**(4), 382–384 (2007).

9. X. Song et al., "Reconstruction for free-space fluorescence tomography using a novel hybrid adaptive finite element algorithm," *Opt. Express* **15**(26), 18300–18317 (2007).

10. R. B. Schulz, J. Ripoll, and V. Ntziachristos, "Experimental fluorescence tomography of tissues with noncontact measurements," *IEEE Trans. Med. Imaging* **23**(4), 492–500 (2004).

11. S. Patwardhan et al., "Time-dependent whole-body fluorescence tomography of probe bio-distributions in mice," *Opt. Express* **13**(7), 2564–2577 (2005).

12. J. Dutta et al., "Illumination pattern optimization for fluorescence tomography: theory and simulation studies," *Phys. Med. Biol.* **55**(10), 2961–2982 (2010).

13. A. Bassi et al., "Spatial shift of spatially modulated light projected on turbid media," *J. Opt. Soc. Am. A* **25**(11), 2833–2839 (2008).

14. C. D'Andrea et al., "Fast 3D optical reconstruction in turbid media using spatially modulated light," *Biomed. Opt. Express* **1**(2), 471–481 (2010).

15. V. Venugopal et al., "Full-field time-resolved fluorescence tomography of small animals," *Opt. Lett.* **35**(19), 3189–3191 (2010).

16. N. Ducros et al., "Fluorescence molecular tomography of an animal model using structured light rotating view acquisition," *J. Biomed. Opt.* **18**(2), 020503 (2013).

17. C. Li et al., "Three-dimensional fluorescence optical tomography in small-animal imaging using simultaneous positron-emission-tomography priors," *Opt. Lett.* **34**(19), 2933–2935 (2009).

18. R. B. Schulz et al., "Hybrid system for simultaneous fluorescence and x-ray computed tomography," *IEEE Trans. Med. Imaging* **29**(2), 465–473 (2010).

19. L. Cao and J. Peter, "Bayesian reconstruction strategy of fluorescence-mediated tomography using an integrated SPECT–CT–OT system," *Phys. Med. Biol.* **55**(9), 2693–2708 (2010).

20. J. Peter, "Triple-modality imaging system," U.S. Patent 2010/0030069 A1 (February 4 2010).

21. L. A. Feldkamp, L. C. Davis, and J. W. Kress, "Practical cone-beam algorithm," *J. Opt. Soc. Am. A* **1**(6), 612–619 (1984).

22. L. Cao and J. Peter, "Slit-slat collimator equipped gamma camera for whole-mouse SPECT–CT imaging," *IEEE Trans. Nucl. Sci.* **59**(3), 530–536 (2012).

23. L. A. Shepp and Y. Vardi, "Maximum likelihood reconstruction for emission tomography," *IEEE Trans. Med. Imaging* **1**(2), 113–122 (1982).

24. L. Cao, M. Breithaupt, and J. Peter, "Geometrical co-calibration of a tomographic optical system with CT for intrinsically co-registered imaging," *Phys. Med. Biol.* **55**(6), 1591–1606 (2010).

25. H. Si and K. Gärtner, "Meshing piecewise linear complexes by constrained Delaunay tetrahedralizations," in *Proc. 14th Int. Meshing Roundtable*, pp. 147–163, Springer (2005).